Spectrum Manipulation for Sound with Effective Gauge Fields in Cascading Temporally Modulated Waveguides

Chengzhi Qin,[1] Yugui Peng,[1,2] Ying Li,[2] Xuefeng Zhu,[1,*] Bing Wang,[1,†] Cheng-Wei Qiu,[2,‡] and Peixiang Lu[1,3,§]

[1] *School of Physics and Wuhan National Laboratory for Optoelectronics, Huazhong University of Science and Technology, Wuhan 430074, China*

[2] *Department of Electrical and Computer Engineering, National University of Singapore, Singapore 119620, Singapore*

[3] *Hubei Key Laboratory of Optical Information and Pattern Recognition, Wuhan Institute of Technology, Wuhan 430205, China*

(Received 11 January 2019; revised manuscript received 12 April 2019; published 6 June 2019)

Spectrum is a basic dimension of waves ranging from electromagnetic to acoustic waves where information can be encoded and multiplexed. The manipulation of the sound spectrum is desirable in applications of acoustic communication and voice encryption, which, however, is challenging to realize. Here, based on temporally modulated waveguides, we create effective gauge fields to generate frequency domain Bloch oscillations (FBOs) to control the spectrum of sound. The modulation can induce mode transitions in the waveguide band and form a discrete frequency lattice where the wave vector mismatch during transitions acts as an effective electric field that drives FBOs. Furthermore, we find the modulation phase accompanying transitions serves as an effective gauge potential that can control the initial oscillation phase. We report that multiple FBOs with judiciously designed oscillation phases can be further cascaded to realize acoustic spectrum reconstruction, unidirectional transduction, and bandwidth engineering. This study reveals the significance of gauge fields in FBOs and functionalizes its cascaded configurations for advanced control of the sound spectrum. This paradigm may find versatile applications in acoustic secure communication, information encryption, and processing.

DOI: 10.1103/PhysRevApplied.11.064012

I. INTRODUCTION

Acoustic waves have found great importance in a variety of wave physics research and practical applications [1–3]. Controlling the spatial degrees of freedom of acoustic waves, such as using sonic crystals, metamaterials, and metasurfaces, has received intensive attention. Examples include acoustic imaging [4–11], vortex [12–16] and accelerating beams [17–20], unidirectional diffraction [21–24], and topological insulators [25–30]. Nevertheless, these studies mainly concern static acoustic systems, in which the sound frequency or spectrum is a conserved quantity. The research of manipulating the sound spectrum is still in its infancy, while it is highly desirable in versatile applications such as in acoustic communication, information encryption, and processing [13]. Previously, the frequency conversion was achieved via an acoustic nonlinear effect, namely, the second harmonic wave generation [31–33]. However, the conversion efficiency is quite low even for high-intensity acoustic waves. Alternatively, a spectrum shift for acoustic waves has also been realized through dynamic scattering from rotating objects [34]. Since this approach depends on the shape and orientation of the scatterers, it is still far from implementing precise control of the sound spectrum.

Recently, the idea of a synthetic frequency dimension has received considerable attention in the contexts of atomic and photonic systems, which provides an alternative mechanism to control the spectra of atoms and photons [35–38]. Typically for photons, the synthetic frequency dimension is usually constructed by inducing photonic transitions among a set of optical modes with equal frequency intervals under external dynamic modulation. Furthermore, by controlling the modulation phase and wave vector, one can also create effective gauge potentials and electric fields in this frequency dimension, thus providing new functionalities to control the spectrum of light [39–44]. Although the concept of a synthetic dimension was first proposed in atomic and photonic systems, the concept itself is universal and should be applicable to all classical wave systems. In this regard, it is ready to

*xfzhu@hust.edu.cn
†wangbing@hust.edu.cn
‡chengwei.qiu@nus.edu.sg
§lupeixiang@hust.edu.cn

introduce the concepts of a synthetic dimension and the associated effective gauge fields to the realm of acoustics, aiming to achieve full control of the sound spectrum.

In this work, we demonstrate the paradigm of a synthetic frequency dimension and effective gauge fields in temporally-modulated acoustic waveguides and realize advanced control of the sound spectrum. Consider that the compressibility of the filling material in an acoustic waveguide is subject to an external modulation, such that mode transitions occur and a synthetic frequency lattice forms. We find that the wave vector mismatch during transitions acts as an effective electric field force that can induce frequency domain Bloch oscillations (FBOs). The initial phase of temporal modulation mimics an effective gauge potential that can control the initial oscillation phase of FBOs. By driving two cascaded FBOs with different oscillation phases in two separated modulation waveguides, we demonstrate a prototype of an acoustic communication system based on the spectrum self-imaging effect. By cascading multiple waveguides with out-of-phase time modulations, we also break the intrinsic localized feature of FBOs and realize spectral unidirectional transduction and bandwidth expansion for sound. Our study reveals the capability of effective gauge fields in the control of the sound spectrum for a plethora of important applications.

II. THE MAIN RESULTS

A. Acoustic frequency domain Bloch oscillations driven by effective gauge fields

We start by revealing the effect of FBOs induced in one time-modulated acoustic waveguide. The waveguide is filled with silicone rubber [45–47], a waterlike ultrasonic material. Suppose the material compressibility is subject to a time modulation $\beta(t)=\beta_0+\Delta\beta\cos(\Omega t+\phi)$, where β_0, $\Delta\beta$, Ω, and ϕ are the background compressibility, modulation amplitude, frequency, and initial phase, respectively. In practice, as shown in Fig. 1(a), the modulation can be realized by compressing the filling medium through piezoelectric actuators [46,47]. The general acoustic wave equations under time modulation are given by [3,46]

$$\begin{cases} \dfrac{\partial\rho(\mathbf{r},t)}{\partial t} = -\rho_0\nabla\cdot\mathbf{v}(\mathbf{r},t), \\ \dfrac{\partial\mathbf{v}(\mathbf{r},t)}{\partial t} = -\dfrac{\nabla p(\mathbf{r},t)}{\rho_0}, \\ \dfrac{\partial\rho(\mathbf{r},t)}{\partial t} = \rho_0\dfrac{\partial[\beta(t)p(\mathbf{r},t)]}{\partial t}, \end{cases} \tag{1}$$

where $\rho(\mathbf{r},t)$, $p(\mathbf{r},t)$, and $\mathbf{v}(\mathbf{r},t)$ are the medium mass density, pressure, and particle velocity. ρ_0 is the time-independent background mass density. The governing equation for the acoustic wave thus reads

$$\nabla^2 p(\mathbf{r},t)-\rho_0\frac{\partial^2}{\partial t^2}[\beta(t)p(\mathbf{r},t)]=0. \tag{2}$$

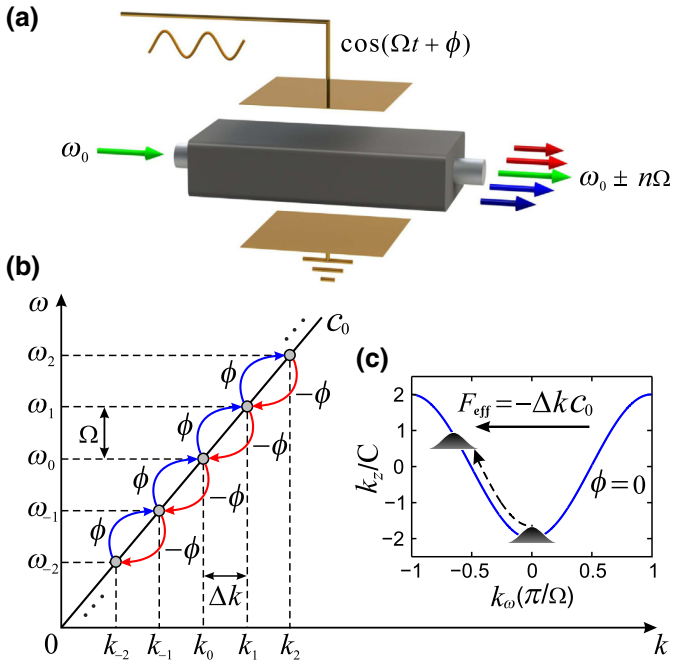

FIG. 1. Schematic sketch of the frequency conversion through FBOs in a temporally-modulated acoustic waveguide filled with silicone rubber. The compressibility of the filling material is subject to a sinusoidal modulation with modulation frequency Ω and initial phase ϕ. The input and output frequencies are denoted by ω_0 and $\omega_0\pm n\Omega$ ($n=0,\ 1,\ 2,\ldots$). (b) Phononic intraband transitions in the linear acoustic waveguide band induced by the temporal modulation. Ω and Δk represent, respectively, the frequency and propagation constant intervals between adjacent ordered modes, with $\pm\phi$ being the phase shift in the upward and downward transitions. c_0 is the sound of speed in the waveguide. (c) Band structure for the modulation-induced frequency lattice with a modulation phase of $\phi=0$, in which FBOs occur under the drive of an effective electric-field force of $F_{\text{eff}}=-\Delta k c_0$.

For simplicity, we consider the one-dimensional case with $\nabla^2=\partial^2/\partial z^2$ and $\mathbf{r}$ replaced by z. As shown in Fig. 1(b), the time-periodic modulation can induce multiple intraband transitions in the linear waveguide band and create an artificial frequency lattice with a lattice constant Ω. The instantaneous pressure field is thus $p(z,t)=\sum_n p_n(z)\exp[i(\omega_n t-k_n z)]$, where $\omega_n=\omega_0+n\Omega$ and $k_n=k_0+n\Delta k$ ($n=0,\ \pm1,\ \pm2,\ldots$) are the angular frequency and wave number of the nth-order fundamental mode. Substituting $p(z,t)$ into Eq. (2), we can derive the coupled-mode equation (see Appendix)

$$i\frac{\partial p_n(z)}{\partial z}=C_n[e^{i(\phi+\Delta kz)}p_{n-1}(z)+e^{-i(\phi+\Delta kz)}p_{n+1}(z)], \tag{3}$$

where $C_n=C=k_0(\Delta\beta/4\beta_0)$ is the coupling strength between adjacent modes in the frequency lattice.

To understand the acoustic spectrum evolution, we first consider the eigen Bloch mode in the frequency lattice, namely, an infinite-width frequency comb

$p_n(z) = p_0 \exp(in\phi_0)\exp(ik_z z)$, where p_0 is the uniform amplitude, ϕ_0 is the Bloch momentum in the frequency dimension, and k_z is the collective propagation constant along the waveguide direction. Plugging the Bloch mode into Eq. (3), we can obtain the lattice effective band structure

$$k_z[\phi_\omega(z)] = -2C\cos[\phi_\omega(z) - \phi], \tag{4}$$

where $\phi_\omega(z) = \phi_0 - \Delta k z$ is the z dependent Bloch momentum. Since $z = c_0 t$, the Bloch momentum also varies in time $\phi_\omega(t) = \phi_0 - \Delta k c_0 t$, where c_0 is the speed of sound in the medium. As denoted in Fig. 1(c), the linearly time-varying Bloch momentum corresponds to a constant electric field force applied along the frequency dimension

$$F_{\text{eff}} = \frac{\partial \phi_\omega(t)}{\partial t} = -\Delta k c_0, \tag{5}$$

which stems from the wave vector mismatch during frequency transitions. Equation (4) shows that $\phi_\omega(z)$ is shifted by ϕ in the band structure, indicating that the modulation phase ϕ plays the role of an effective gauge potential through

$$\int_{\omega_n}^{\omega_{n+1}} A_{\text{eff}} d\omega = \phi, \tag{6}$$

from which we have $A_{\text{eff}} = \phi/\Omega$. Denoting $\phi_\omega(z) = k_\omega(z)\Omega$, the band structure can be rewritten as $k_z[k_\omega(z)] = -2C\cos[(k_\omega(z) - A_{\text{eff}})\Omega]$. The band structure shift induced by the gauge potential is analogous to the situation where the kinetic momentum of an electron is substituted by the conical momentum in the presence of an electromagnetic vector potential [48,49]. For the input of a real finite-width Bloch-mode wave packet centered at an initial Bloch momentum ϕ_0, the group velocity in the frequency lattice is z periodic, $v_g(z) = -\partial k_z[k_\omega(z)]/\partial k_\omega(z) = -2C\Omega\sin(\phi_0 - \Delta k z - \phi)$, which gives rise to a frequency shift $\omega(z) = \omega(0) + \int_0^z v_g(z')dz'$

$$\omega(z) = \omega(0) + \frac{2C\Omega}{\Delta k}[\cos(\phi - \phi_0) - \cos(\Delta k z + \phi - \phi_0)], \tag{7}$$

where $\omega(0)$ denotes the initial central frequency. The center-of-mass of the wave packet undergoes an oscillatory motion in the frequency lattice, which is FBOs. The corresponding oscillation period is $Z_B = 2\pi/|\Delta k| = 2\pi c_0/|F_{\text{eff}}|$, which is inversely proportional to the magnitude of the driving force. Furthermore, we point out that the initial oscillation phase is determined by the gauge potential, namely, the initial modulation phase ϕ. In the following, we shall exploit this gauge degree of freedom by cascading multiple FBOs with different oscillation phases, aiming to provide new functionalities of acoustic spectrum manipulation that are unattainable in a single FBO process.

B. Spectrum reconstruction for acoustic communication with two cascaded FBOs

In this section, we will apply two cascaded FBOs to the scenarios of acoustic secure communications. A typical communication system usually comprises three basic parts: the modulation, demodulation modules, and the in-between transmission channel. As shown schematically in Fig. 2(a), the two waveguides modulated with the same frequency Ω but different phases (ϕ_1 and ϕ_2) can function as the modulation and demodulation modules, with the central unmodulated waveguide serving as the transmission channel. Moreover, we assume the information to be transmitted is encoded in the spectrum of an acoustic signal. To achieve secure communication, the spectrum of the input signal should be deformed through the first FBO process in the modulation module such that the encoded information can be protected from being detected in the transmission channel. In the demodulation module, the deformed spectrum should then return to its input formula through the second FBO process. The question lies in how to design the two modulated waveguide lengths and modulation phases such that spectrum reconstruction can be realized for an arbitrarily input acoustic signal.

To reveal the conditions for spectrum reconstruction in the proposed communication system, we first consider a frequency comb wave packet incidence in the

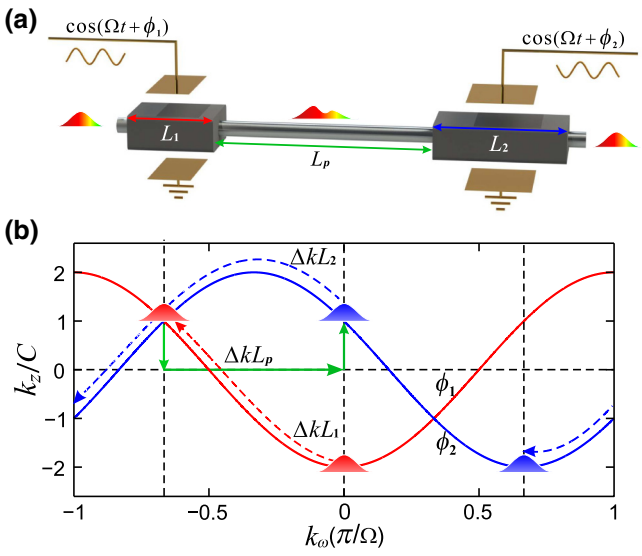

FIG. 2. (a) Schematic diagram of the frequency multiplexed acoustic communication system, which consists of two modulated waveguides separated by an unmodulated transmission channel. The two waveguides with lengths of $L_1 = Z_B/3$ and $L_2 = 2Z_B/3$ are modulated with the same frequency Ω but different phases of $\phi_1 = 0$ and $\phi_2 = 2\pi/3$. The length of the unmodulated channel is $L_p = Z_B/3$, where $Z_B = 2\pi/|\Delta k|$ is the period of the FBOs. (b) The variation of Bloch momentum of an input frequency comb wave packet during the cascaded FBOs in the two modulated waveguides.

system. As shown in Fig. 2(b), the wave packet with initial Bloch momentum ϕ_0 manifests FBOs (represented by the dashed red curve) in the encoding waveguide, with the instantaneous Bloch momentum being $\phi_\omega(z)=\phi_0-\Delta kz$, which reaches $\phi_0-\Delta kL_1$ at its end. In the central unmodulated waveguide, though no FBOs occur, the phase difference between adjacent order modes still accumulates due to the presence of waveguide dispersion (denoted by the green arrows). Here, we assume the channel waveguide length is L_p and the phase difference thus evolves into $\phi_0-\Delta kL_1+\Delta kL_p$ at its end. When entering the decoding waveguide, FBOs restart and the Bloch momentum again manifests a linear shift as $\phi_\omega(z)=(\phi_0-\Delta kL_1+\Delta kL_p)-\Delta k(z-L_1-L_p)=\phi_0+2\Delta kL_p-\Delta kz$ (represented by the blue dashed curve). Due to the distinct gauge potentials in the two modulation waveguides, the Bloch momentum undergoes different shifts in the two phase reference frames of ϕ_1 and ϕ_2. Thus, we can obtain the relative Bloch momentum $\phi_\omega(z)-\phi_m$ $(m=1,2)$ in the two waveguides

$$\phi_{\omega,m}(z)=\begin{cases}(\phi_0-\Delta kz)-\phi_1, & (m=1)\\ (\phi_0+2\Delta kL_p-\Delta kz)-\phi_2, & (m=2)\end{cases}. \tag{8}$$

To realize the spectrum reconstruction at the output port of the whole system, two conditions must be simultaneously satisfied. Condition 1: The Bloch momentum at the output port of the encoding waveguide should equal that at the input port of the decoding waveguide, namely, $\phi_{\omega,1}(L_1)=\phi_{\omega,2}(L_1+L_p)$. Condition 2: The total lengths of encoding and decoding waveguides should be integer multiples of the Bloch period. The two conditions can be summarized as

$$\begin{cases}\delta\phi=\Delta\phi-\Delta\phi_p=0,\\ L_1+L_2=vZ_B,\ (v=1,2,\ldots),\end{cases} \tag{9}$$

where $\Delta\phi=\phi_2-\phi_1$ and $\Delta\phi_p=\Delta kL_p$. In Eq. (9), Condition 1 indicates that the modulation phase difference in the two modulation waveguides should be compensated by the propagation phase difference between adjacent ordered modes in the central transmission channel. Condition 2 guarantees the recovery of Bloch momentum after two FBO processes. Only when the two conditions are simultaneously satisfied will the output spectrum perfectly return to its input state. For a general case, the band structures and group velocities in the two modulation waveguides are $k_{z,m}[k_\omega(z)]=-2C\cos[\phi_\omega(z)-\phi_m]$ and $v_{g,m}(z)=-2C\Omega\sin[\phi_\omega(z)-\phi_m]$ with $m=1,2$, leading to the frequency comb evolution

$$\omega(z)=\begin{cases}\omega(0)+\dfrac{2C\Omega}{\Delta k}[\cos(\phi_1-\phi_0)-\cos(\Delta kz+\phi_1-\phi_0)], & (0\le z\le L_1)\\ \omega(L_1), & (L_1\le z\le L_1+L_p)\\ \omega(L_1)+\dfrac{2C\Omega}{\Delta k}[\cos(\Delta kL_1-\Delta kL_p+\phi_2-\phi_0) & \\ \quad-\cos(\Delta kz-2\Delta kL_p+\phi_2-\phi_0)]. & (L_1+L_p\le z\le L_1+L_p+L_2)\end{cases} \tag{10}$$

When Condition 2 is satisfied, namely, $\Delta k(L_1+L_2)=2\pi$, the output frequency center is

$$\omega_{\text{out}}=\omega(0)-\frac{8C\Omega}{\Delta k}\sin\left(\frac{\Delta kL_1}{2}\right)\sin\left(\frac{\delta\phi}{2}\right)\times\cos\left(\phi_1-\phi_0+\frac{\Delta kL_1}{2}+\frac{\delta\phi}{2}\right). \tag{11}$$

If Condition 1 is also satisfied with $\delta\phi=0$, we have $\omega_{\text{out}}=\omega(0)$. The frequency comb center comes back to its initial position, verifying the two conditions in Eq. (9) for spectrum reconstruction.

The above theoretical analysis can be verified with numerical simulations of acoustic spectrum evolution. The simulations are performed by solving coupled-mode Eq. (3) under different input conditions. Here, we choose $\rho_0=990\,\text{kg m}^{-3}$ and $\beta_0=9.824\times10^{-10}\ \text{Pa}^{-1}$ for silicone rubber, such that $c_0=1/(\rho_0\beta_0)^{1/2}=1014\,\text{m s}^{-1}$ [45–47]. The compressibility modulation depth is chosen as $\Delta\beta/\beta_0=0.05\ll1$, indicating that the modulation can be regarded as a weak perturbation. Other parameters are $\omega_0/2\pi=\omega(0)/2\pi=50$ kHz, $\Omega/2\pi=200$ Hz, $L_1=Z_B/3$, $L_2=2Z_B/3$ $(L_1+L_2=Z_B)$, and $L_p=Z_B/3$ $(\Delta\phi_p=2\pi/3)$. Figure 3(a) shows the output spectrum evolution versus the phase difference $\delta\phi=\Delta\phi-\Delta\phi_p$ under a frequency comb input with a sound pressure distribution of $p_n(0)=\exp[-(n\Omega/W)^2]\exp(in\phi_0)$, where $W=5\Omega$ is the width of the Gaussian envelope and $\phi_0=0$ is the initial Bloch momentum. The envelope manifests sinusoidal variation with respect to $\delta\phi$, in good agreement with the theoretical result denoted by the blue curve prediction by Eq. (11). Then we input a single frequency instead of a frequency comb into the system. As shown in Fig. 3(b), the output spectrum evolution manifests a breathing pattern as $\delta\phi$ varies, which returns to a single frequency as $\delta\phi=0$, also verifying the condition in Eq. (9).

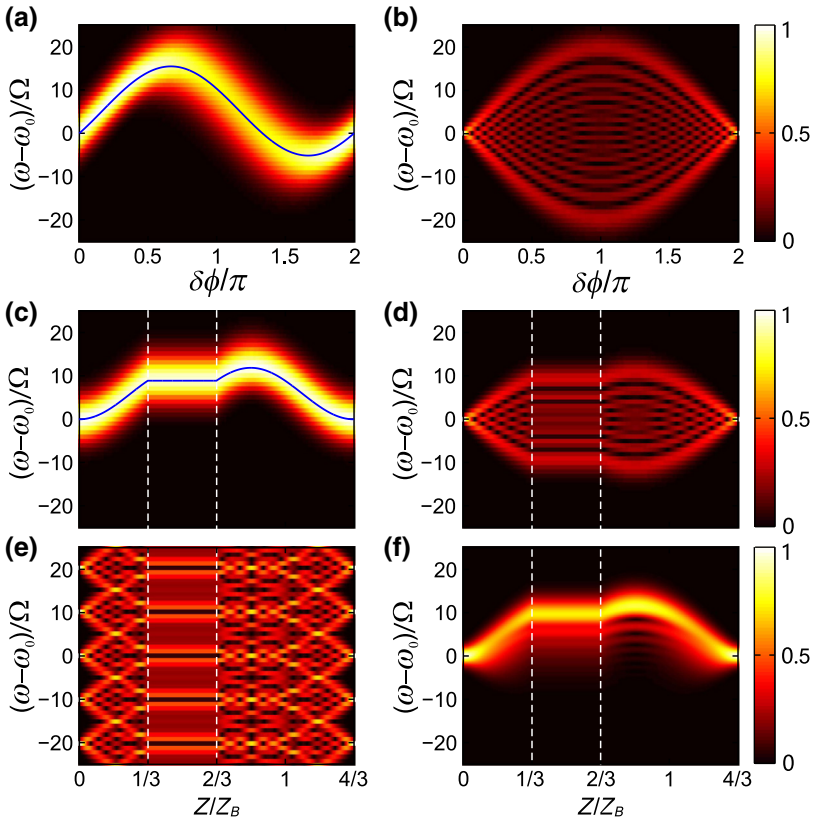

FIG. 3. (a) Acoustic spectrum evolution versus the phase difference of $\delta\phi = \Delta\phi - \Delta\phi_p$ for a frequency comb input with an initial Bloch momentum $\phi_0 = 0$ and comb width of $W = 5\Omega$. The blue curve represents the theoretical result predicted by Eq. (11). (b) Acoustic spectrum evolution versus $\delta\phi$ for a single frequency input. Spectrum evolutions in the proposed acoustic communication system with the input of (c) a frequency comb, (d) a single frequency, (e) a periodic discrete spectrum, and (f) a continuous spectrum under the condition of $\delta\phi = 0$, respectively. The blue curve in (c) denotes the theoretical trajectory of the frequency comb envelope evolution predicted by Eq. (10). In (f), the width of the continuous Gaussian spectrum wave packet is $W = 2\Omega$. The white dashed lines denote the boundaries among the encoding, unmodulated, and decoding waveguides.

To visualize the process of spectrum reconstruction, we fix $\delta\phi = 0$ and input different kinds of spectra into the system. Figure 3(c) denotes the spectrum evolution for a frequency comb input under the modulation phase of $\phi_1 - \phi_0 = 0$. The frequency comb manifests cosine oscillation during FBOs in the encoding waveguide, remains unchanged in the transmission channel, and exhibits oscillation again in the decoding waveguide, ultimately returning to the input state. The envelope evolution trajectory also agrees well with the theoretical prediction in Eq. (10). In Fig. 3(d), a single frequency instead of a frequency comb is incident into the system, which also returns to a single frequency at the output port. In terms of Fourier analysis, a single frequency can be regarded as the superposition of all frequency comb components with Bloch momentum covering the entire Brillouin zone. Since all frequency combs are reconstructed, the superimposed single frequency will exhibit self-focusing.

More generally, since the spectrum reconstruction relies only on the conditions of Eq. (9), it should apply to arbitrarily input spectra, including both discrete and continuous ones. To verify this, we also input a periodic spectrum with a frequency interval of 10Ω into the system. As shown in Fig. 3(e), these equally distributed frequencies can be regarded as the different channels in the frequency division multiplexing communication systems. The periodic spectrum manifests channel crosstalk in the encoding waveguide and remains unchanged in the center transmission waveguide, ultimately returning to its initial state at the output port. Thus, we can reconstruct a periodic spectrum through the cascaded FBOs. Moreover, we input a Gaussian pulse into the system, which possesses a continuous Gaussian spectrum. The width of the Gaussian spectrum envelope is $W = 2\Omega$ and the modulation phase with respect to the pulse arrival time is chosen as $\phi_1 = 0$. As shown in Fig. 3(f), the spectrum manifests bandwidth expansion in the encoding waveguide and then bandwidth compression in the decoding waveguide, which can also be perfectly reconstructed at the output port.

To further confirm the above calculated results obtained by solving coupled-mode Eq. (3), we also perform first-principle simulations by solving the time-dependent wave equation of Eq. (2) with the finite-element method (FEM) based on COMSOL Multiphysics. For comparison purposes, both the coupled-mode and FEM simulation results are shown in Fig. 4. Here, we choose a frequency comb and single frequency inputs in Figs. 4(a) and 4(b), corresponding to those in Figs. 3(c) and 3(d). The modulation depth in Fig. 4 is $\Delta\beta/\beta_0 = 0.01$, with all other parameters kept the same as those in Fig. 3. For the frequency comb input shown in Fig. 4(a), the FEM simulation spectra at $z = 0$, L_1, $L_1 + L_p$, and $L_1 + L_p + L_2$ are represented by the blue curves, which agree well with the coupled-mode simulation results denoted by the green dots. Moreover, both the FEM and coupled-mode simulation results show that the frequency comb evolves along the theoretical trajectory

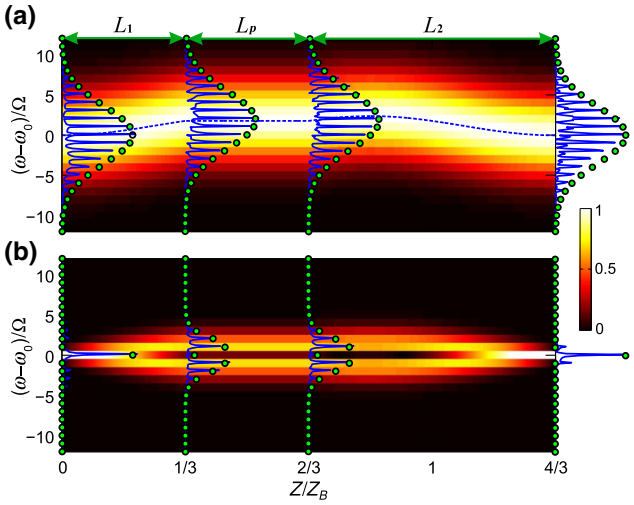

FIG. 4. The comparisons between the coupled-mode equation simulation results using Eq. (2) and the FEM simulation results using Eq. (3) under (a) a frequency comb and (b) a single frequency input. In both (a) and (b), the blue curves denote the FEM simulation spectra at $z=0$, L_1, L_1+L_p, and $L_1+L_p+L_2$, while the green dots represent the corresponding coupled-mode simulation spectra. The background thermal figures in (a) and (b) denote the whole spectrum evolutions.

predicted by Eq. (10), further validating the theoretical analysis. In Fig. 4(b), we input a single frequency into the system and both the FEM and coupled-mode simulations show that the single frequency evolves into a frequency comb in the encoding waveguide and remains unchanged in the central transmission channel, ultimately converging back onto a single frequency at the end of the decoding waveguide. The FEM simulations further confirm the spectrum reconstruction functionality for a secure communication system.

As indicated in Sec. A, the modulation phase acts as an effective gauge potential that can control the initial oscillation phase of FBOs, so we now exploit the modulation phase to manipulate the spectrum evolution processes. Figures 5(a)–5(d) illustrate the frequency comb evolutions as the modulation phases are chosen as $\phi_1-\phi_0=0,\pi,\pi/2$, and $-\pi/2$, respectively. Other parameters are the same as those in Fig. 3. The theoretical trajectories are denoted by the blue curves, which agree well with the simulated results. The evolution trajectory for $\phi_1-\phi_0=0$ manifests mirror symmetry with respect to that for $\phi_1-\phi_0=\pi$, indicating the opposite frequency shifts during each FBO process. This mirror symmetry also applies to the cases for $\phi_1-\phi_0=\pi/2$ and $-\pi/2$. In Figs. 5(e)–5(h), we input a continuous Gaussian spectrum instead of frequency combs into the system. The modulation phases with respect to the pulse arrival time are chosen as $\phi_1=0,\pi,\pi/2$, and $-\pi/2$, respectively. Similar to the situations of frequency comb inputs, the continuous spectrum evolutions also manifest mirror symmetries for $\phi_1-\phi_0=0$ and π as well as for $\phi_1-\phi_0=\pi/2$ and $-\pi/2$.

Now we discuss the influence of the initial width of the incident spectrum on its evolution process. In Figs. 6(a)–6(c), the input Gaussian spectra have widths of $W=\Omega$, 2Ω, and 5Ω, respectively. As the width increases, the spectrum experiences greater bandwidth expansion during propagation. This can be interpreted in terms

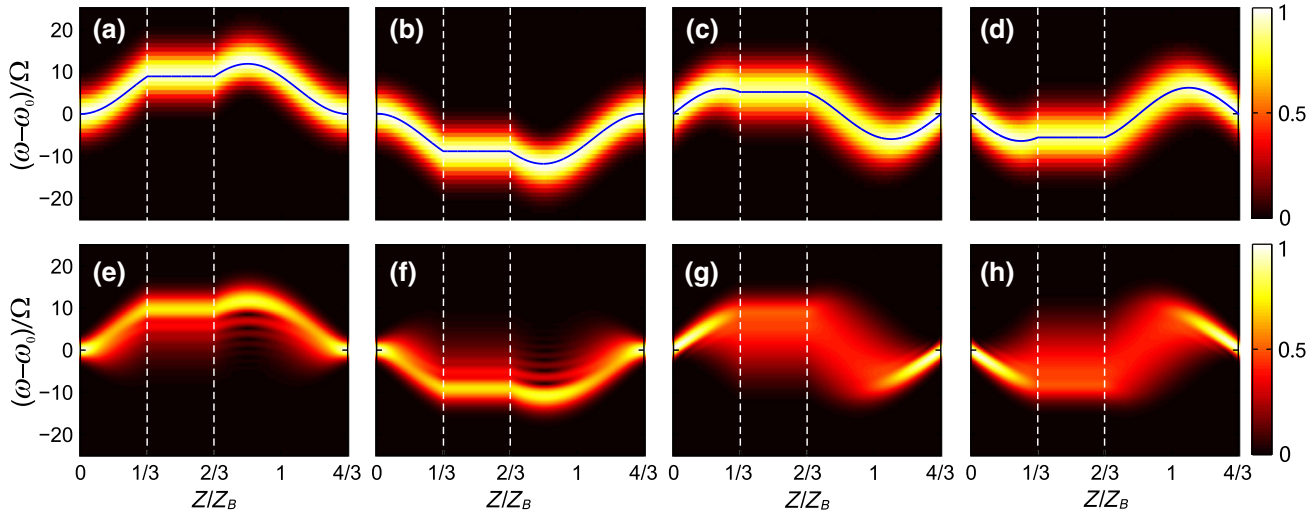

FIG. 5. (a)-(d) Influence of modulation phase $\phi_1-\phi_0$ on the spectrum evolution for a frequency comb input during cascaded FBOs. The modulation phase is (a) $\phi_1-\phi_0=0$, (b) $\phi_1-\phi_0=\pi$, (c) $\phi_1-\phi_0=\pi/2$, and (d) $\phi_1-\phi_0=-\pi/2$, respectively. All other parameters are kept the same as those in Fig. 3(c). The blue curve in each panel denotes the theoretical evolution trajectory of the frequency comb envelope. (e)-(h) Spectrum evolutions for a continuous Gaussian spectrum input under different modulation phases of $\phi_1=0,\pi,\pi/2$, and $-\pi/2$, respectively. The modulation phase here is defined with respect to the pulse arrival time. The white dashed lines denote the boundaries between the encoding, unmodulated, and decoding waveguides.

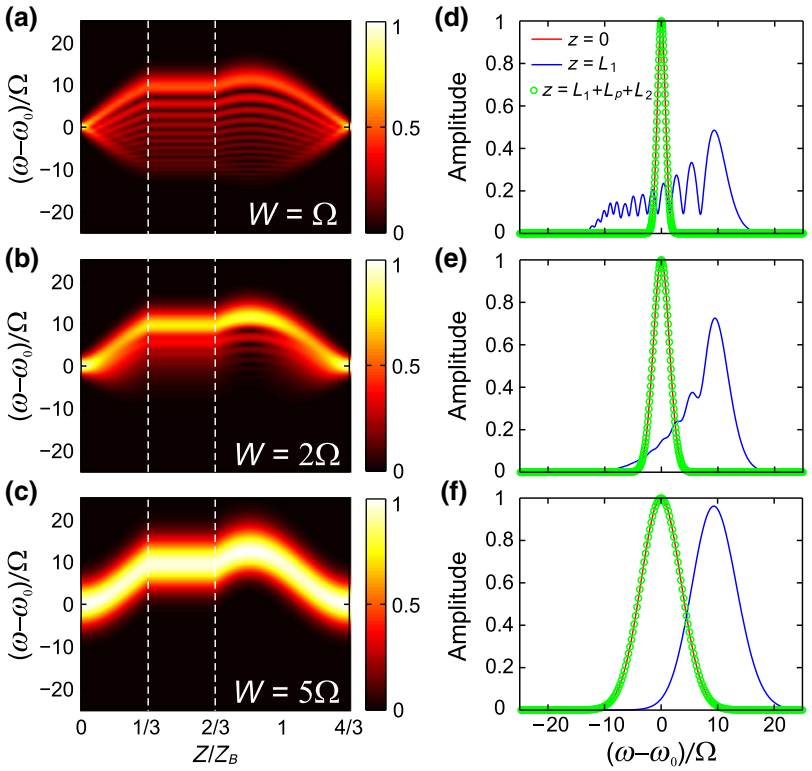

FIG. 6. (a)-(c) Influence of the initial spectrum width on the frequency evolution for a continuous Gaussian spectrum input. The initial width of the Gaussian spectrum envelope is (a) $W=\Omega$, (b) $W=2\Omega$, and (c) $W=5\Omega$, respectively, where $\Omega=2\pi\times 200\,\mathrm{Hz}$ is the modulation frequency. All other parameters are kept the same as those in Fig. 3(f). (d)-(f) One-dimensional spectrum distributions at distances of $z=0$, L_1, and $L_1+L_p+L_2$ in (a)-(c), respectively.

of the uncertainty principle: A spectrum wave packet with a narrower bandwidth contains more Bloch momentum components in the Brillouin zone, giving rise to more obvious bandwidth expansion during propagation. Figures 6(d)–6(f) show the one-dimensional spectra at $z=0$, L_1, and $L_1+L_2+L_p$, all of which manifest spectrum reconstructions at the output port. The narrower spectrum also manifests a more obvious spectrum shift and distortion in the propagation process.

Finally, we will discuss the advantages of cascaded FBOs for acoustic secure communications. In principle, a freely propagating waveguide can also transmit an acoustic signal without any spectrum distortion. However, the information encoded in the spectrum can be detected during propagation if there exists only a free transmission channel. Therefore, the modulation and demodulation modules are necessary to encode and decode the transmitted information. In addition, due to the periodic nature of FBOs, one FBO process is, in principle, enough to achieve spectrum reconstruction. Nevertheless, in practical situations, especially for long-distance acoustic communication, one FBO process requires a modulation waveguide with sufficient length. This scheme could dramatically increase the system complexity and cost. In view of all of the above drawbacks for a freely propagating waveguide and one FBO process, it is most appropriate to use the modulation-transmission-demodulation configuration to realize acoustic secure communications.

C. Spectrum transduction and band engineering with multiple cascaded FBOs

Due to the periodically oscillatory nature for FBOs [50], the frequency shift in a single FBO process is limited within the range of $|\Delta\omega|_{\max}=4C\Omega/|\Delta k|$. To break this intrinsic localized feature of FBOs and realize spectrum directional transduction, we can cascade multiple FBOs with appropriately designed oscillation phases. For simplicity, we consider M modulation waveguides are directly cascaded without unmodulated channels in between. The length and modulation phase of the mth waveguide are L_m and ϕ_m, for which the band structure and group velocity are $k_{z,m}(\phi_\omega(z))=-2C\cos[\phi_\omega(z)-\phi_m]$ and $v_{g,m}(z)=-2C\Omega\sin[\phi_0-\Delta kz-\phi_m]$, $(m=1,2,\ldots,M)$. The evolution trajectory of the frequency comb is

$$\omega_m(z)=\begin{cases}\omega(0)+\dfrac{2C\Omega}{\Delta k}[\cos(\phi_1-\phi_0)-\cos(\Delta kz+\phi_1-\phi_0)], & (m=1)\\ \omega\left(\sum\limits_{i=1}^{m-1}L_i\right)+\dfrac{2C\Omega}{\Delta k}\left[\cos\left(\sum\limits_{i=1}^{m-1}\Delta kL_i+\phi_m-\phi_0\right)-\cos(\Delta kz+\phi_m-\phi_0)\right]. & (m\geq 2)\end{cases} \tag{12}$$

To realize unidirectional spectrum transduction, we can fix each waveguide length as $L_m = Z_B/2$ and choose out-of-phase modulations $\Delta\phi = \phi_{m+1} - \phi_m = \pi$ in adjacent waveguides. For an initial phase difference $\phi_1 - \phi_0 = 0$ or π, the frequency comb will exhibit a unidirectional blue or red shift

$$\omega_m(z) = \omega(0) \pm \frac{4C\Omega(m-1)}{\Delta k} \pm \frac{2C\Omega}{\Delta k}\begin{cases} 1-\cos(\Delta k z) & (m \text{ is odd}) \\ 1+\cos(\Delta k z) & (m \text{ is even}) \end{cases}, \quad (13)$$

where we choose $+(-)$ for $\phi_1 - \phi_0 = 0(\pi)$. For both cases, the total accumulated frequency shift is $|\Delta\omega|_{\max} = \omega_m(mZ_B/2) - \omega(0) = 4MC\Omega/\Delta k$, which is proportional to the number of modulation waveguides. On the contrary, for $\phi_1 - \phi_0 = \pm\pi/2$, the frequency shift will vanish with $|\Delta\omega| = 0$. For other choices of phase differences $\phi_1 - \phi_0 \neq 0$, π, or $\pm\pi/2$, the frequency shift satisfies $0 < |\Delta\omega| < |\Delta\omega|_{\max}$, which can be precisely tuned by varying the modulation phases. The theoretical analysis has also been verified by simulations in Fig. 7, where we fix $M = 4$ and $L_m = Z_B/2$. Figure 7(a) shows the spectrum evolution for a frequency comb input as $\phi_1 - \phi_0 = 0$. The spectrum experiences a directional blue shift with vanished bandwidth expansion, consistent with the theoretical trajectory denoted by the blue curve predicted by Eq. (13). While for $\phi_1 - \phi_0 = \pi/2$ shown in Fig. 7(b), the frequency shift vanishes and the bandwidth expansion reaches the maximum. By choosing $\phi_1 - \phi_0 = \pi/3$ in Fig. 7(c), both frequency shift and bandwidth expansion exist, where the amounts are less than the cases of $\phi_1 - \phi_0 = 0$ or $\pi/2$. Finally, we input a single frequency into the system, as shown in Fig. 7(d), and the spectrum manifests discrete diffraction during propagation, with the bandwidth reaching the maximum of $2|\Delta\omega|_{\max} = 32C\Omega/|\Delta k|$ at the output port.

The functionalities of spectrum transduction and bandwidth expansion can also be generalized to continuous spectra. Figures 8(a)–8(c) denote the spectrum evolutions under the modulation phase of $\phi_1 = 0$ with the initial spectrum widths of $W = 1\Omega$, 2Ω, and 5Ω, respectively. As the initial width increases, the spectrum expansion will decrease, giving rise to better directionality for the spectrum transduction. In Figs. 8(d)–8(f), the modulation phase is chosen as $\phi_1 = \pi/2$ with all other parameters kept unchanged. The Gaussian spectra with initial widths of $W = 1\Omega$, 2Ω, and 5Ω all experience band expansion during propagation. As the initial width decreases, the bandwidth expansion becomes more obvious. For a sufficiently narrow width, the spectrum evolution will approach the situation of a single frequency input as shown in Fig. 7(d). Thus, to obtain better directionality for the spectrum transduction, one should choose a spectrum with

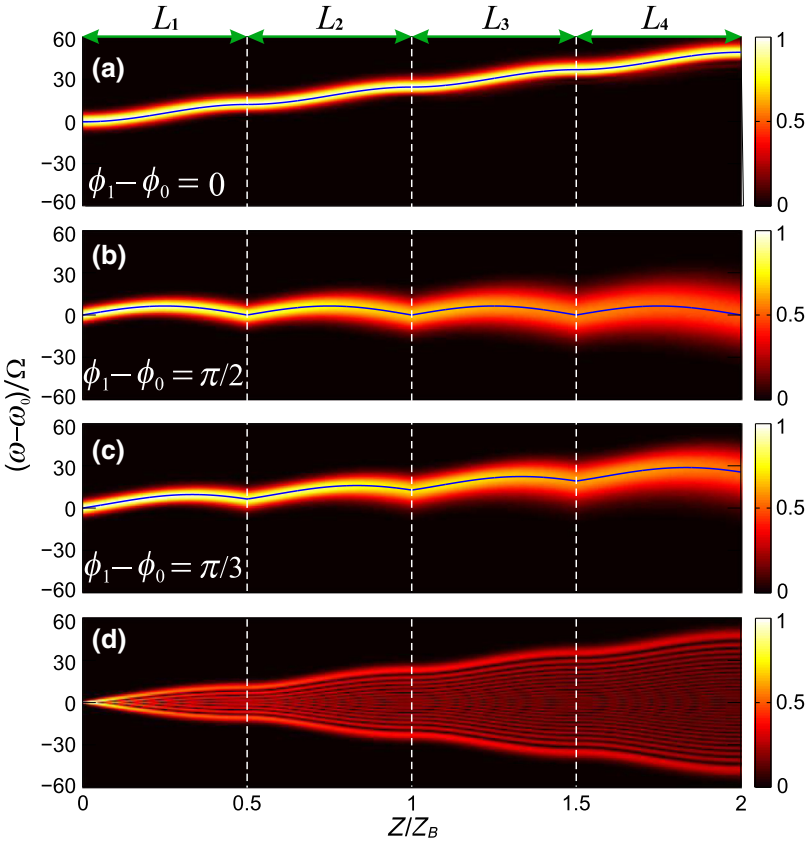

FIG. 7. Acoustic spectrum evolutions for a frequency comb input with $\phi_0 = 0$ and $W = 5\Omega$ in four cascading waveguides under out-of-phase modulation. The initial phase differences are (a) $\phi_1 - \phi_0 = 0$, (b) $\phi_1 - \phi_0 = \pi/2$, and (c) $\phi_1 - \phi_0 = \pi/3$, respectively. The length of each waveguide is fixed as $L_m = Z_B/2$ ($m = 1, 2, 3, 4$). The blue curves in (a), (b), and (c) denote the theoretical trajectories of the acoustic frequency comb envelopes. (d) Acoustic spectrum evolution for a single frequency input. The white dashed lines denote the boundaries of the four-section time-modulated waveguides.

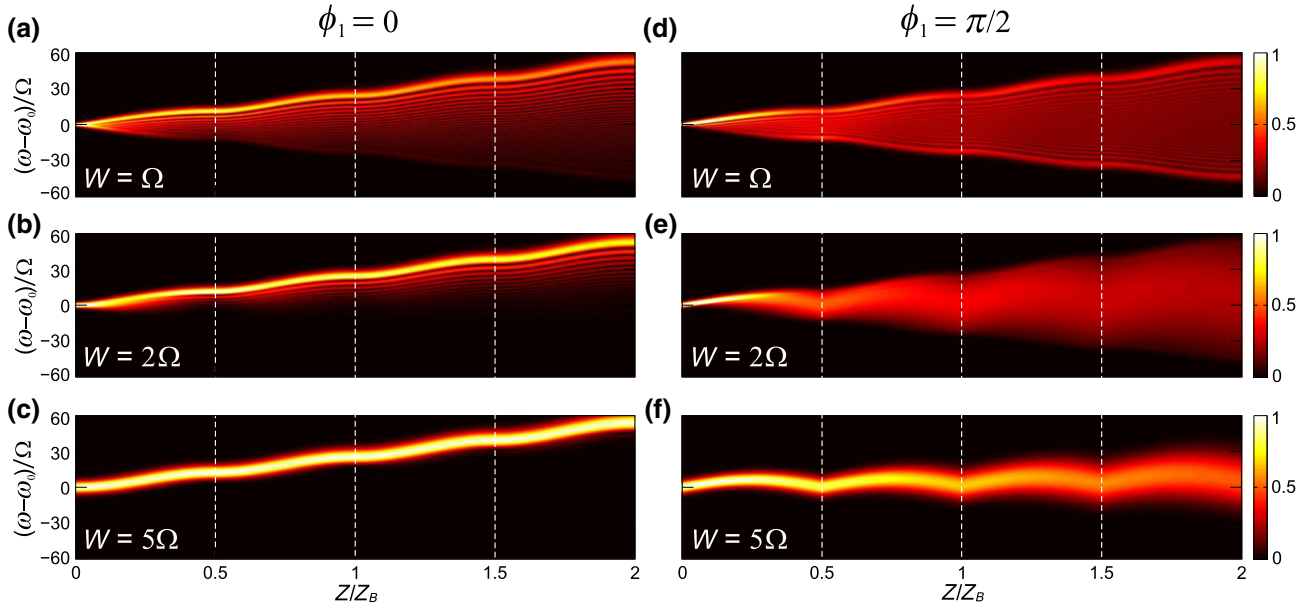

FIG. 8. Influence of initial spectrum width on the frequency transduction and bandwidth expansion in four cascading modulation waveguides. (a)-(c) Directional blue shifts for a continuous Gaussian spectrum input under $\phi_1 = 0$ and $\Delta\phi = \phi_{m+1} - \phi_m = \pi$, where ϕ_1 is the modulation phase in the first waveguide with respect to the spectrum arrival time and $\Delta\phi$ is the modulation phase difference between adjacent waveguides. The width of the Gaussian spectrum envelope is (a) $W = \Omega$, (b) $W = 2\Omega$, and (c) $W = 5\Omega$, respectively, where $\Omega = 2\pi \times 200$ Hz is the modulation frequency. All other parameters are kept the same as those in Fig. 6. (d)-(f) Spectrum evolutions for a continuous Gaussian spectrum input for the modulation phase of $\phi_1 = \pi/2$ in the first waveguide with respect to the pulse arrival time.

a broad bandwidth. On the contrary, to achieve a more obvious bandwidth expansion, the initial spectrum width should be chosen to be as narrow as possible. Thus, by exploiting multiple cascaded FBOs, we can achieve flexible control over the both the spectrum shifts and bandwidth expansion for acoustic signals.

III. CONCLUSIONS

In summary, we establish a framework to control a sound spectrum through cascaded FBOs in time-modulation waveguide systems. The wave vector mismatch in frequency transition acts as an effective electric field that drives FBOs, and the modulation phase plays the role of an effective gauge potential, which determines the initial oscillation phase of FBOs. Utilizing a pair of time-modulation waveguides with judiciously designed modulation phases and lengths, we demonstrate acoustic secure communication via spectrum self-imaging. By cascading multiple waveguides under out-of-phase time modulations, we realize unidirectional spectrum shift and bandwidth expansion. Finally, since all the effects do not rely on the explicit choice of incident spectrum, our work may find important applications in spectrum engineering with the operation bandwidth ranging from audible up to ultrasonic regimes.

ACKNOWLEDGMENTS

This work is supported by the 973 Program (Grant No. 2014CB921301), the National Natural Science Foundation of China (Grants No. 11674117, No. 11674119, No. 11690030, and No. 11690032). Y.P. acknowledges financial support from the China Scholarship Council (CSC).

Chengzhi Qin and Yugui Peng contributed equally to this work.

APPENDIX: COUPLED-MODE EQUATION OF FBOS

Here, we provide the detailed derivation for the coupled-mode equation of Eq. (3) and discuss the algorithm of numerically solving the equation. As shown in the main text, the acoustic pressure distribution under time modulation is given by

$$\nabla^2 p(\mathbf{r},t) - \rho_0 \frac{\partial^2}{\partial t^2}[\beta(t) p(\mathbf{r},t)] = 0, \tag{A1}$$

where the compressibility is assumed to be subjected to a sinusoidal modulation

$$\beta(t) = \beta_0 + \Delta\beta \cos(\Omega t + \phi). \tag{A2}$$

For a one-dimensional case with $\nabla^2 = \partial^2/\partial z^2$ and $\mathbf{r}$ replaced by z, the modulation can induce acoustic intraband transitions in the linear waveguide band, giving rise to the acoustic pressure

$$p(z,t) = \sum_n p_n(z) \exp[i(\omega_n t - k_n z)], \tag{A3}$$

where $\omega_n = \omega_0 + n\Omega$ and $k_n = k_0 + n\Delta k$ ($n = 0, \pm 1, \pm 2, \ldots$) are the angular frequency and the propagation constant of the nth-order fundamental mode. Substituting Eqs. (A2) and (A3) into (A1), we have the following equation

$$\frac{\partial^2 p(z,t)}{\partial z^2} - \rho_0\beta_0\frac{\partial^2 p(z,t)}{\partial t^2} = \rho_0\Delta\beta\frac{\partial^2}{\partial t^2}[\cos(\Omega t + \phi)p(z,t)]. \tag{A4}$$

By applying a slowly varying amplitude approximation and $\rho_0\beta_0\omega_n^2 - k_n^2 = \omega_n^2/c_0^2 - k_n^2 = 0$, the left side of Eq. (A4) is

$$\sum_n \left[\frac{\partial^2 p_n(z)}{\partial z^2} - 2ik_n\frac{\partial p_n(z)}{\partial z} + \left(\frac{\omega_n^2}{c_0^2} - k_n^2\right)\right] e^{i(\omega_n t - k_n z)} = -\sum_n 2ik_n\frac{\partial p_n(z)}{\partial z}e^{i(\omega_n t - k_n z)}. \tag{A5}$$

With $\omega_n \pm \Omega = \omega_{n\pm1}$ and $k_n \pm \Delta k = k_{n\pm1}$, the right-hand side of Eq. (A4) is

$$\begin{aligned}
&\rho_0\Delta\beta\frac{\partial^2}{\partial t^2}\left\{\frac{1}{2}[e^{i(\Omega t+\phi)} + e^{-i(\Omega t+\phi)}]\sum_n p_n(z)e^{i(\omega_n t - k_n z)}\right\} \\
&= \frac{\rho_0\Delta\beta}{2}\frac{\partial^2}{\partial t^2}\sum_n p_n(z)\left(e^{i(\omega_n+\Omega)t}e^{-i(k_n+\Delta k)z}e^{i(\phi+\Delta kz)}\right. \\
&\quad \left. + e^{i(\omega_n-\Omega)t}e^{-i(k_n-\Delta k)z}e^{-i(\phi+\Delta kz)}\right) \\
&= -\frac{\rho_0\Delta\beta}{2}\sum_n p_n(z)\left(\omega_{n+1}^2 e^{i(\omega_{n+1}t - k_{n+1}z)}e^{i(\phi+\Delta kz)}\right. \\
&\quad \left. + \omega_{n-1}^2 e^{i(\omega_{n-1}t - k_{n-1}z)}e^{-i(\phi+\Delta kz)}\right).
\end{aligned} \tag{A6}$$

Substituting $(n \pm 1)$ with n, we have

$$\sum_n p_n(z)\omega_{n\pm1}^2 e^{i(\omega_{n\pm1}t - k_{n\pm1}z)} = \sum_n p_{n\mp1}(z)\omega_n^2 e^{i(\omega_n t - k_n z)}. \tag{A7}$$

Therefore, we can obtain the coupled-mode equation

$$i\frac{\partial p_n(z)}{\partial z} = C_n[e^{i(\phi+\Delta kz)}p_{n-1}(z) + e^{-i(\phi+\Delta kz)}p_{n+1}(z)], \tag{A8}$$

where the coupling strength between the nth and $(n \pm 1)$th-order mode is given by

$$C_n = \frac{\rho_0\Delta\beta\omega_n^2}{4k_n} = \frac{\Delta\beta}{4\beta_0}k_n. \tag{A9}$$

Since $\Omega \ll \omega_0$, the coupling strength for each order can be considered as a constant $C_n = C = k_0(\Delta\beta/4\beta_0)$. By truncating the order to the maximum $n = M$ and denoting $|\varphi(z)\rangle = [p_1(z), p_2(z), \ldots, p_N(z)]^{\mathrm{T}}$ with $N = 2M + 1$, the coupled-mode equations can be rewritten as a time-dependent Schrödinger equation

$$i\frac{\partial|\varphi(z)\rangle}{\partial z} = \mathbf{H}(z)|\varphi(z)\rangle, \tag{A10}$$

with the z dependent matrix $\mathbf{H}(z)$ given by

$$\mathbf{H}(z) = \begin{pmatrix}
0 & Ce^{-i(\phi+\Delta kz)} & 0 & \cdots & 0 & 0 \\
Ce^{i(\phi+\Delta kz)} & 0 & Ce^{-i(\phi+\Delta kz)} & \cdots & 0 & 0 \\
0 & Ce^{i(\phi+\Delta kz)} & 0 & \cdots & 0 & 0 \\
\vdots & \vdots & \vdots & \ddots & \vdots & \vdots \\
0 & 0 & 0 & \cdots & 0 & Ce^{-i(\phi+\Delta kz)} \\
0 & 0 & 0 & \cdots & Ce^{i(\phi+\Delta kz)} & 0
\end{pmatrix}. \tag{A11}$$

The dynamics of FBOs can thus be obtained by numerically solving Eq. (A10).

[1] L. Lin, P. Hu, J. Shi, C. M. Appleton, K. Maslov, L. Li, R. Zhang, and L. V. Wang, Single-breath-hold photoacoustic computed tomography of the breast, Nat. Commun. **9**, 2352 (2018).

[2] H. S. Park and B. K. Oh, Damage detection of building structures under ambient excitation through the analysis of the relationship between the modal participation ratio and story stiffness, J. Sound Vib. **418**, 122 (2018).

[3] F. B. Jensen, W. A. Kuperman, M. B. Porter, and H. Schmidt, *Computational Ocean Acoustics* (Springer, New York/Dordrecht/Heidelberg/London, 2011).

[4] X. Zhu, B. Liang, W. Kan, X. Zou, and J. Cheng, Acoustic Cloaking by a Superlens with Single-Negative Materials, Phys. Rev. Lett. **106**, 014301 (2011).

[5] M. D. Guild, M. R. Haberman, and A. Alù, Plasmonic-type acoustic cloak made of a bilaminate shell, Phys. Rev. B **86**, 104302 (2012).

[6] C. Shen, J. Xu, N. X. Fang, and Y. Jing, Anisotropic Complementary Acoustic Metamaterial for Canceling out Aberrating Layers, Phys. Rev. X **4**, 041033 (2014).

[7] X. Zhu, H. Ramezani, C. Shi, J. Zhu, and X. Zhang, PT -Symmetric Acoustics, Phys. Rev. X **4**, 031042 (2014).

[8] W. Kan, V. M. García-Chocano, F. Cervera, B. Liang, X. Zou, L. Yin, J. Cheng, and J. Sánchez-Dehesa, Broadband Acoustic Cloaking within an Arbitrary Hard Cavity, Phys. Rev. Appl. **3**, 064019 (2015).

[9] J. Li, L. Fok, X. Yin, G. Bartal, and X. Zhang, Experimental demonstration of an acoustic magnifying hyperlens, Nat. Mater. **8**, 931 (2009).

[10] Z. Liang and J. Li, Extreme Acoustic Metamaterial by Coiling Up Space, Phys. Rev. Lett. **108**, 114301 (2012).

[11] N. I. Zheludev and Y. S. Kivshar, From metamaterials to metadevices, Nat. Mater. **11**, 917 (2012).

[12] X. Jiang, Y. Li, B. Liang, J. C. Cheng, and L. Zhang, Convert Acoustic Resonances to Orbital Angular Momentum, Phys. Rev. Lett. **117**, 034301 (2016).

[13] C. Shi, M. Dubois, Y. Wang, and X. Zhang, High-speed acoustic communication by multiplexing orbital angular momentum, Proc. Natl. Acad. Sci. USA **114**, 7250 (2017).

[14] X. Jiang, B. Liang, J. C. Cheng, and C. Qiu, Twisted acoustics: Metasurface-enabled multiplexing and demultiplexing, Adv. Mater. **30**, 1800257 (2018).

[15] W. Li, M. Ke, S. Peng, F. Liu, C. Qiu, and Z. Liu, Rotational manipulation by acoustic radiation torque of high-order vortex beams generated by an artificial structured plate, Appl. Phys. Lett. **113**, 051902 (2018).

[16] H. Tang, Z. Chen, N. Tang, S. Li, Y. Shen, Y. Peng, X. Zhu, and J. Zang, Hollow-out patterning ultrathin acoustic metasurfaces for multifunctionalities using soft fiber/rigid bead networks, Adv. Funct. Mater. **28**, 1801127 (2018).

[17] P. Zhang, T. Li, J. Zhu, X. Zhu, S. Yang, Y. Wang, X. Yin, and X. Zhang, Generation of acoustic self-bending and bottle beams by phase engineering, Nat. Commun. **5**, 4316 (2014).

[18] X. Zhu, K. Li, P. Zhang, J. Zhu, J. Zhang, C. Tian, and S. Liu, Implementation of dispersion-free slow acoustic wave propagation and phase engineering with helical-structured metamaterials, Nat. Commun. **7**, 11731 (2016).

[19] U. Bar-Ziv, A. Postan, and M. Segev, Observation of shape-preserving accelerating underwater acoustic beams, Phys. Rev. B **92**, 100301 (2015).

[20] Y. Li and M. B. Assouar, Three-dimensional collimated self-accelerating beam through acoustic metascreen, Sci. Rep. **5**, 17612 (2015).

[21] X. Zhu, X. Zou, B. Liang, and J. Cheng, One-way mode transmission in one-dimensional phononic crystal plates, J. Appl. Phys. **108**, 124909 (2010).

[22] X. Li, X. Ni, L. Feng, M. Lu, C. He, and Y. Chen, Tunable Unidirectional Sound Propagation through a Sonic-Crystal-Based Acoustic Diode, Phys. Rev. Lett. **106**, 084301 (2011).

[23] N. Nadkarni, A. F. Arrieta, C. Chong, D. M. Kochmann, and C. Daraio, Unidirectional Transition Waves in Bistable Lattices, Phys. Rev. Lett. **116**, 244501 (2016).

[24] T. Liu, X. Zhu, F. Chen, S. Liang, and J. Zhu, Unidirectional Wave Vector Manipulation in Two-Dimensional Space with an All Passive Acoustic Parity-Time-Symmetric Metamaterials Crystal, Phys. Rev. Lett. **120**, 124502 (2018).

[25] Z. Yang, F. Gao, X. Shi, X. Lin, Z. Gao, Y. Chong, and B. Zhang, Topological Acoustics, Phys. Rev. Lett. **114**, 114301 (2015).

[26] A. B. Khanikaev, R. Fleury, S. H. Mousavi, and A. Alù, Topologically robust sound propagation in an angular-momentum-biased graphene-like resonator lattice, Nat. Commun. **6**, 8260 (2015).

[27] Y. Peng, C. Qin, D. Zhao, Y. Shen, X. Xu, M. Bao, H. Jia, and X. Zhu, Experimental demonstration of anomalous Floquet topological insulator for sound, Nat. Commun. **7**, 13368 (2016).

[28] C. He, X. Ni, H. Ge, X. Sun, Y. Chen, M. Lu, X. Liu, and Y. Chen, Acoustic topological insulator and robust one-way sound transport, Nat. Phys. **12**, 1124 (2016).

[29] J. Lu, C. Qiu, L. Ye, X. Fan, M. Ke, F. Zhang, and Z. Liu, Observation of topological valley transport of sound in sonic crystals, Nat. Phys. **13**, 369 (2016).

[30] H. Xue, Y. Yang, F. Gao, Y. Chong, and B. Zhang, Acoustic higher-order topological insulator on a kagome lattice, Nat. Mater. **18**, 108 (2018).

[31] B. Liang, B. Yuan, and J. C. Cheng, Acoustic Diode: Rectification of Acoustic Energy Flux in One-Dimensional Systems, Phys. Rev. Lett. **103**, 104301 (2009).

[32] B. Liang, X. S. Guo, J. Tu, D. Zhang, and J. C. Cheng, An acoustic rectifier, Nat. Mater. **9**, 989 (2010).

[33] N. Boechler, G. Theocharis, and C. Daraio, Bifurcation-based acoustic switching and rectification, Nat. Mater. **10**, 665 (2011).

[34] Q. Wang, Y. Yang, X. Ni, Y. Xu, X. Sun, Z. Chen, L. Feng, X. Liu, M. Lu, and Y. Chen, Acoustic asymmetric transmission based on time-dependent dynamical scattering, Sci. Rep. **5**, 10880 (2015).

[35] A. Celi, P. Massignan, J. Ruseckas, N. Goldman, I. B. Spielman, G. Juzeliūnas, and M. Lewenstein, Synthetic Gauge Fields in Synthetic Dimensions, Phys. Rev. Lett. **112**, 043001 (2014).

[36] B. K. Stuhl, H.-I. Lu, L. M. Aycock, D. Genkina, and I. B. Spielman, Visualizing edge states with an atomic Bose gas in the quantum Hall regime, Science **349**, 6255 (2015).

[37] M. Mancini, G. Pagano, G. Cappellini, L. Livi, M. Rider, J. Catani, C. Sias, P. Zoller, M. Inguscio, M. Dalmonte, and L. Fallani, Observation of chiral edge states with neutral fermions in synthetic Hall ribbons, Science **349**, 1510 (2015).

[38] T. Ozawa, H. M. Price, N. Goldman, O. Zilberberg, and I. Carusotto, Synthetic dimensions in integrated photonics: From optical isolation to four-dimensional quantum Hall physics, Phys. Rev. A **93**, 043827 (2016).

[39] L. Yuan, Q. Lin, M. Xiao, and S. Fan, Synthetic dimension in photonics, Optica **5**, 1396 (2018).

[40] L. Yuan, Y. Shi, and S. Fan, Photonic gauge potential in a system with a synthetic frequency dimension, Opt. Lett. **41**, 741 (2016).
[41] L. Yuan and S. Fan, Bloch oscillation and unidirectional translation of frequency in a dynamically modulated ring resonator, Optica **3**, 1014 (2016).
[42] B. A. Bell, K. Wang, A. S. Solntsev, D. N. Neshev, A. A. Sukhorukov, and B. J. Eggleton, Spectral photonic lattices with complex long-range coupling, Optica **4**, 1433 (2017).
[43] C. Qin, Feng Zhou, Y. Peng, D. Sounas, X. Zhu, B. Wang, J. Dong, X. Zhang, A. Alù, and P. Lu, Spectrum Control through Discrete Frequency Diffraction in the Presence of Photonic Gauge Potentials, Phys. Rev. Lett. **120**, 133901 (2018).
[44] C. Qin, L. Yuan, B. Wang, S. Fan, and P. Lu, Effective electric-field force for a photon in a synthetic frequency lattice created in a waveguide modulator, Phys. Rev. A **97**, 063838 (2018).
[45] D. L. Folds, Speed of sound and transmission loss in silicone rubbers at ultrasonic frequencies, J. Acoust. Soc. Am. **56**, 1295 (1974).
[46] R. Fleury, D. L. Sounas, and A. Alù, Subwavelength ultrasonic circulator based on spatiotemporal modulation, Phys. Rev. B **91**, 174306 (2015).
[47] R. Fleury, A. B. Khanikaev, and A. Alù, Floquet topological insulators for sound, Nat. Commun. **7**, 11744 (2016).
[48] J. Dalibard, F. Gerbier, G. Juzeliūnas, and P. Öhberg, Colloquium: Artificial gauge potentials for neutral atoms, Rev. Mod. Phys. **83**, 1523 (2011).
[49] Q. Lin and S. Fan, Light Guiding by Effective Gauge Field for Photons, Phys. Rev. X **4**, 031031 (2014).
[50] T. Hartmann, F. Keck, H. J. Korsch, and S. Mossmann, Dynamics of Bloch oscillations, New J. Phys. **6**, 2 (2004).